Ultrasonics 129 (2023) 106908

Contents lists available at ScienceDirect

Ultrasonics

journal homepage: www.elsevier.com/locate/ultras

Synthetic radial aperture focusing to regulate manual volumetric scanning for economic transrectal ultrasound imaging

Hyunwoo Song [a], Jeeun Kang [b,*], Emad M. Boctor [a,b,*]

[a] Department of Computer Science, Whiting School of Engineering, the Johns Hopkins University, Baltimore, MD 21218, USA
[b] Laboratory for Computational Sensing and Robotics, Whiting School of Engineering, the Johns Hopkins University, Baltimore, MD 21218, USA

ARTICLE INFO

Keywords:
Transrectal ultrasound
Synthetic radial aperture focusing
Volumetric
Image Reconstruction

ABSTRACT

In this paper, we present a volumetric transrectal ultrasound (TRUS) imaging under the presence of radial scanning angle disorientation (SAD) in a resource-limited diagnostic setting. Herein, we test our hypothesis that a synthetic radial aperture focusing (TRUS-rSAF) technique, in which a radial plane in target volume is reconstructed by coherent compounding of multiple transmittance/reception events, will reject a randomized SAD in a free-hand scanning setup based on external angular tracking. Based on an analytical model of the TRUS-rSAF technique, we first tested specific scenarios using a clinically available TRUS transducer under different SADs in a range of normal distributions (σ = 0.1°, 0.2°, 0.5°, 1°, 2°, and 5°). We found a benefit of the TRUS-rSAF technique for higher robustness when the SAD is contained within the radial synthetic aperture window, i.e., ±0.71° from a target scanning angle. However, no enhancement was found in spatial resolution because of the limited transmit beam field of the clinical TRUS transducer, limiting the synthetic aperture window. We further evaluated the TRUS-rSAF technique with a modified TRUS transducer for an extended synthetic aperture window to test whether higher spatial resolution and robustness to SAD can be obtained in the same evaluation setup. Widening of the synthetic aperture window (±3.54°, ± 5.91°, ± 8.27°, ± 10.63°, ± 12.99°, ± 15.35°) resulted in proportional enhancements of spatial resolution, but it also progressively built up sidelobe artifacts due to randomized synthesis with limited phase cancellations. The results suggest the need for careful calibration of the TRUS-rSAF technique to enable TRUS imaging with free-hand radial scanning and external angle tracking in resource-limited settings.

1. Introduction

Transrectal ultrasound (TRUS) imaging is an effective clinical tool for prostate cancer localization, biopsy guidance, and post-treatment surveillance [1,2]. For several decades, 2-dimensional (2-D) TRUS imaging has been performed as a standard protocol using a 1-D linear or curved array transducer, but it has been criticized for its high dependency on the clinician's dexterity and subjective anatomic interpretation. Clinical urology reports the advantages of 3-D TRUS imaging, delineating comprehensive anatomic context in the prostate, renal and pelvic regions [3,4]. A conventional volumetric TRUS scanning mechanism in modern ultrasound (US) imaging devices is straightforward. Each radial plane is reconstructed by a lateral beamforming process in a single transmittance/reception event using the 1-D linear array, and the process repeats after a step rotation until filling the entire target volume [5]. A volumetric scanning using a TRUS transducer fully integrated with a rotational scanning actuator and encoder is a standard to guarantee a sufficient radial scanning accuracy (<0.001°). The US imaging platform should also support a dedicated hardware control for such a motorized TRUS transducer. The configuration is required to avoid 'scanning-angle disorientation' (SAD), which indicates any discrepancy between a current scanning angle and a recognized angle when filling the target volume. In simple calculation, only 1° of SAD could already produce 1.75-mm radial distortion at 100-mm imaging depth. Such errors will repeatedly appear at each scanning angle, resulting in a substantial distortion of the volumetric TRUS image. However, its substantial complexity and cost have been a barrier for resource- and budget-limited settings such as rural hospitals and/or developing countries. Healthcare providers in those settings may appreciate a volumetric imaging option requiring only a simple 1-D TRUS transducer without any expensive actuator and encoder. Therefore, there is an imminent need for an effective yet economic framework to alleviate the

---

* Corresponding authors.
E-mail addresses: kangj@jhu.edu (J. Kang), eboctor@jhu.edu (E.M. Boctor).

https://doi.org/10.1016/j.ultras.2022.106908
Received 30 June 2022; Received in revised form 18 October 2022; Accepted 27 November 2022

SAD in an economic volumetric TRUS imaging at minimal hardware cost.

There have been numerous spatial calibration methods for volume reconstruction and multi-modal registration. Guo *et al.* [6] and Parrot *et al.* [7] presented interpolation-based reconstruction methods to suppress volumetric scanning errors based on morphologic features in medical images. However, diagnostic US imaging has low contrast resolution with unpredictable speckle patterns, so such image-based methods would quickly become vulnerable to external noises. On the other hand, Janvier *et al.* [8] proposed a robot-assisted 3-D US imaging system in which a calibrated robot arm reduced sequential volume scanning error compared to a free-hand scanning method. However, such robot-attached systems necessitate a substantial alteration in current clinical protocol and repetitive calibrations, which would bother clinical procedures and become a hurdle for practical translation into practice.

Synthetic aperture focusing (SAF) techniques have been highlighted in the modern US imaging field, which coherently compounds time-multiplexed transmittance/reception events in an extended aperture at a specific target pixel, which leads to higher spatial resolution and signal sensitivity along with enhanced texture uniformity[9]. Most prior theoretical investigations on the SAF techniques have only considered lateral scanning scenarios, leaving translational or rotational scanning scenarios unexplored. It is primarily because the adjacent scanning

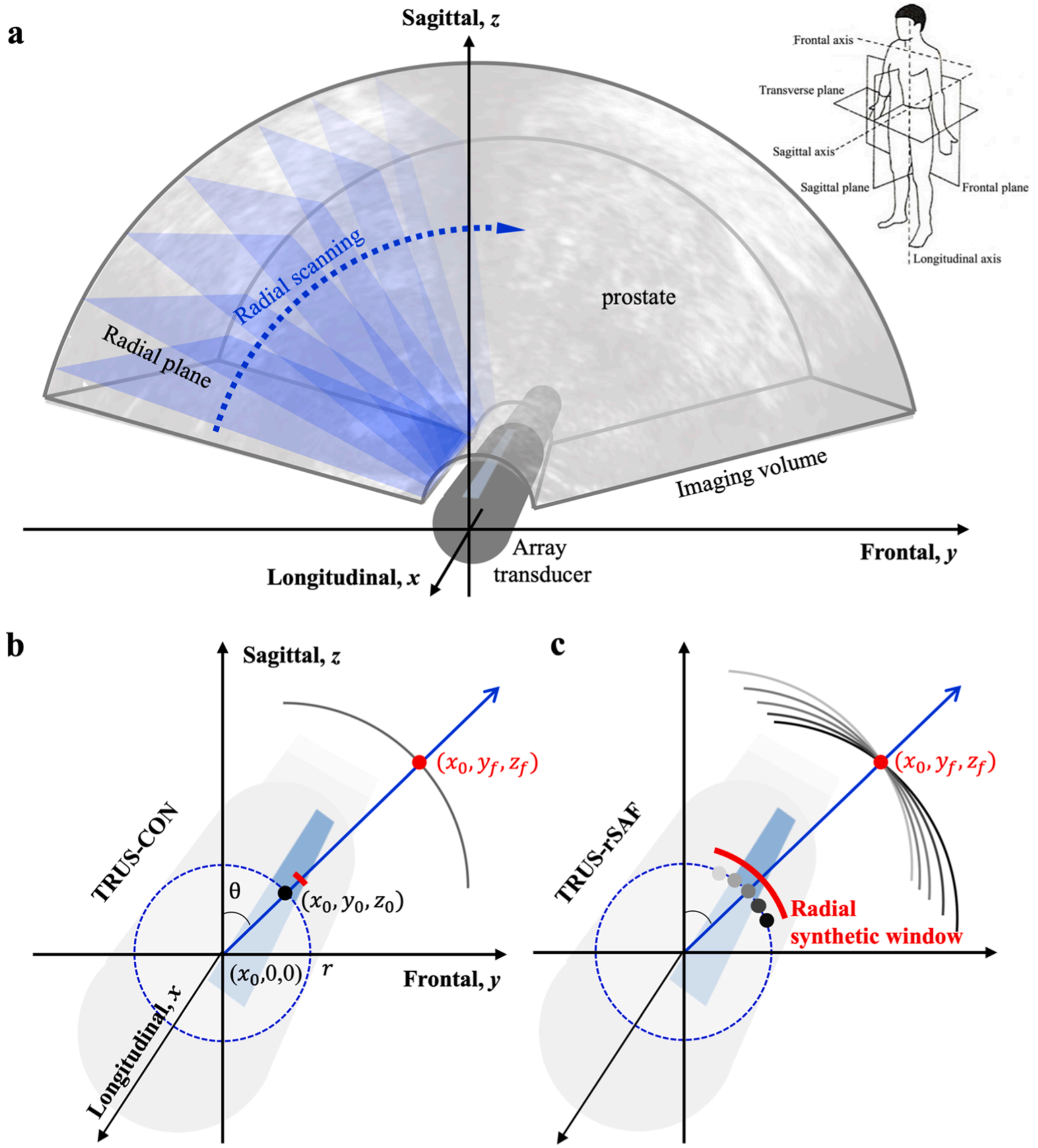

Fig. 1. 3-D TRUS scanning and beamforming processes. (a) Sequential radial scanning to cover the target imaging volume. The radial transmit aperture and focusing in (b) the conventional TRUS imaging (TRUS-CON) technique and (c) the proposed synthetic radial aperture focusing (TRUS-rSAF) technique. Receive beamforming at a target pixel (x_0, y_f, z_f) in a specific lateral cross-section of the TRUS transducer ($x = x_0$). Blue arrowed lines indicate the target scanning angle θ. Red bars indicate effective radial synthetic window. Gray arcs crossing the target pixel indicate the spherical wavefront from radial origin(s) at (x_0, y_0, z_0). Each wavefront is with different focusing delays to be synthesized at (x_0, y_f, z_f). The TRUS-CON technique only has one wavefront to reconstruct a radial plane. r is the TRUS transducer radius. (For interpretation of the references to colour in this figure legend, the reader is referred to the web version of this article.)

planes in these scenarios will have limited overlap in acoustic fields due to the fixed elevation lens focusing of the US arrays [10,11]. To navigate this unexplored gap, our group recently proposed an analytical model of the synthetic radial aperture focusing technique for volumetric TRUS imaging (TRUS-rSAF), providing a theoretical framework to maximize imaging performance [12]. However, the theoretical efficacy of our previous study was limited in a scenario assuming no SAD presence during a volumetric TRUS scanning. Also, we hypothesize that the coherent compounding of the TRUS-rSAF technique will alleviate the SAD-induced artifacts without any additional processes.

Herein, we further evolve the theoretical framework of the TRUS-rSAF technique to reflect the randomized SAD during a volumetric scanning using a clinically available 1-D linear TRUS array, assuming manual volumetric scanning under external tracking at low accuracy. We first built a theoretical model of the SAD-reflected TRUS-rSAF imaging, followed by comprehensive performance comparisons to a negative control case without the rSAF technique (TRUS-CON), where a transmittance/reception event will constitute a single radial plane in the target volume. The performance evaluation is based on acoustic beam profile analysis in the frontal-sagittal domain with different SAD ranges with normal distributions: $\sigma = 0.1^\circ$, 0.2°, 0.5°, 1°, 2°, and 5°. The high robustness of the TRUS-rSAF technique is statistically evaluated with 100-times SAD permutations. Imaging performance is characterized by point-spread function (PSF) and tissue-mimicking phantom simulations using the Field-II tool [13,14]. Lastly, we further analyzed a TRUS-rSAF technique with optimized transducer specifications [12] to test whether spatial resolution and SAD robustness can be concurrently improved.

2. Fundamental theory and implementation

2.1. Synthetic radial aperture focusing sequence in volumetric TRUS imaging

Fig. 1 overviews the volumetric TRUS scanning and beamforming processes. Note that SAD is not reflected in this introductory figure. The fundamentals of mechanical 3-D scanning in the TRUS-CON and TRUS-rSAF techniques are identical, filling up the target volume with a sequential scanning of radial planes (Fig. 1a). An acoustic transmit/receive event will be performed for each target angle θ, and lateral beamforming reconstructs each radial plane (blue planes in Fig. 1a). The process will be repeated until the target volume is filled. However, there is a considerable difference in the reconstruction processing pipelines of the TRUS-CON and TRUS-rSAF techniques. Fig. 1b,c show the simplified acoustic field for the TRUS-CON and -rSAF techniques at a specific lateral position of the TRUS transducer (x_0). The TRUS-CON technique will reconstruct a single target radial plane in a single transmittance/reception event without further processing among adjacent planes (Fig. 1b). In this case, each target pixel (x_0, y_f, z_f) is reconstructed by a small effective aperture data using a single element height. On the other hand, the TRUS-rSAF technique will temporarily store the adjacent radial planes obtained by multiple transmittance/reception events, followed by their coherent synthesis with individual delay compensation processes to the target pixel (x_0, y_f, z_f) (Fig. 1c). Such a SAF process brings potential benefits of enhanced spatial resolution and signal-to-noise ratio (SNR) respectively due to the broadened effective aperture and coherent compounding. In this study, we use this coherent averaging mechanism of the TRUS-rSAF technique to alleviate the image distortions caused by randomized SADs and further test whether the TRUS-rSAF technique can concurrently enhance image quality.

2.2. Field analysis model

Fig. 2 overviews the 2-D field analysis models of the TRUS-rSAF techniques with and without SAD in the frontal-sagittal space. We develop the analytical model in a specific longitudinal cross-section at x_0, and omit the longitudinal index for a simpler presentation. Fig. 2a first illustrates the ideal 2-D model of the TRUS-rSAF technique, where the acoustic element rotates along with the origin with the rotating radius $r = \sqrt{y_0^2 + z_0^2}$, and the acoustic wave propagates along with a scanning angle $\theta = \sin^{-1}\alpha$. The effective radial synthetic window function $p(\alpha)$ and a synthetic time delay function $\tau(\alpha)$ at the focal point (y_f, z_f) are given by

$$p(\alpha) = rect\left(\frac{\alpha}{\alpha_{max}}\right) \tag{1-1}$$

$$\tau(\alpha) = e^{-jkR_f} = e^{-jk\sqrt{(y_f - r\alpha)^2 + (z_f - r\beta)^2}} \tag{1-2}$$

where $\beta = \cos\theta$ and $\alpha_{\max}$ is the maximum scanning angle. Based on the

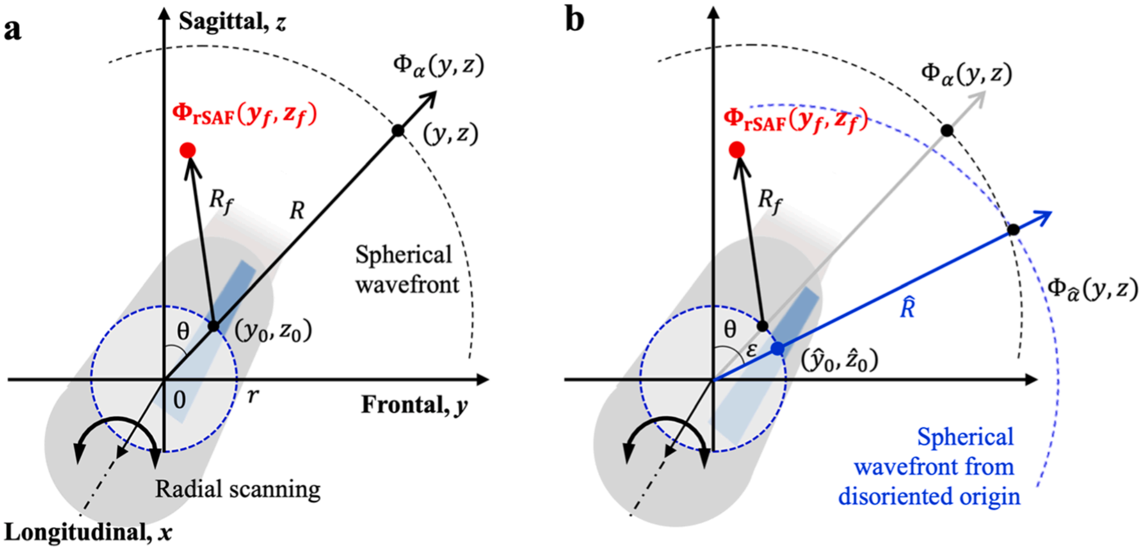

Fig. 2. 2-dimensional theoretical field analysis models of TRUS-rSAF technique in frontal-sagittal plane over a specific longitudinal cross-section at x_0. Derivations (a) without and (b) with scanning-angle disorientation (SAD). Blue dotted line indicates a spherical wavefront from disoriented origin $(\hat{y}_0, \hat{z}_0)$. Red dot indicates the synthetic focusing pixel (y_f, z_f); (y_0, z_0) is an element position; and $\theta = \sin^{-1}\alpha$. (For interpretation of the references to colour in this figure legend, the reader is referred to the web version of this article.)

theory in our previous study, the resultant synthetic acoustic beam pattern focused on the focal point (y_f, z_f) can be derived as

$$\Psi_{rSAF}\left(y_f, z_f\right) = c_0 sinc\left(\frac{r\alpha_{max}}{\lambda z_f} y^{'}\right) \tag{2}$$

where λ is the wavelength of the transmitted acoustic wave, $y^{'} = y - y_f$ and $c_0 = \alpha_{max} e^{jk\frac{y^2 - y_f^2}{2z_f}}$ with $k = 2\pi/\lambda$. The derived beam pattern defines the first null point of the mainlobe (i.e., $y^{'}_{\mathrm{ML}}$) by

$$y^{'}_{ML} = \frac{\lambda z_f}{r\alpha_{max}} \tag{3}$$

More practically, a discrete synthesis of N radial planes with an interval $\Delta\alpha$ was considered. Hence, the resultant beam pattern was derived as

$$\Psi_s\left(y_f, z_f\right) = e^{jk\frac{y^2 - y_f^2}{2z_f}} \sum_{n=0}^{N-1} e^{-jk\frac{r\alpha_n}{z_f} y} = c_0^{'} \frac{sin\pi \frac{rN\Delta\alpha}{\lambda z_f} y}{sin\pi \frac{r\Delta\alpha}{\lambda z_f} y} \tag{4}$$

where $c_0^{'} = e^{jk\frac{y^2 - y_f^2 + y^{'}\alpha_{\max}}{2z_f}}$. Similarly, the null point of the mainlobe and the center positions of grating lobes ($y_s^{'}$ML and $y_s^{'}$GL, respectively) are obtained from (4):

$$y_s^{'}ML = \frac{\lambda z_f}{rN\Delta\alpha} \tag{5-1}$$

$$y_s^{'}GL = \frac{\lambda z_f}{r\Delta\alpha} n (n = 1, 2, 3, \cdots) \tag{5-2}$$

2.3. Revised SAD-reflected field analysis model

We further evolved the analytical TRUS-rSAF model to reflect the SAD. Fig. 2b illustrates a scenario where a randomized SAD (i.e., ε) is presented. The revised position of the acoustic element (y_0, z_0) due to ε is given by

$$(\widehat{y}_0, \widehat{z}_0) = (r\widehat{\alpha}, r\widehat{\beta}) \tag{6}$$

where $\widehat{\alpha} = \alpha + \varepsilon$ and $\widehat{\beta} = 1 - (\alpha + \varepsilon)^2/2$, assuming no mean bias (μ = 0). Here, we assume that $\alpha = \theta$ based on the small-angle approximation (i.e., $\theta \cong \sin\theta$) [15]. Our plan to have a more practical SAD model is described in the Discussion section. The corresponding change in the transmit beam pattern is given by

$$\Psi_{\widehat{\alpha}}(y, z) = e^{jk\widehat{R}} = e^{jk\sqrt{(y - r\widehat{\alpha})^2 + (z - r\widehat{\beta})^2}} \tag{7}$$

The synthetic transmit beam pattern, acquired by coherent compounding of multiple transmitted waves, is given by

$$\widehat{\Psi}_{rSAF}\left(y_f, z_f, \varepsilon\right) = \int_{-\infty}^{\infty} p(\alpha)\tau(\alpha)\Psi_{\widehat{\alpha}}(y, z) d\alpha = \int_{-\infty}^{\infty} p(\alpha) e^{jk\left(\widehat{R} - R_f\right)} d\alpha \tag{8}$$

It is important to note here that $p(\alpha)$ and $\tau(\alpha)$ does not reflect SAD because the current SAD is blinded on the beamformer side. After mathematical expansion, Eq. (8) can be reformulated as

$$\widehat{\Psi}_{rSAF}\left(y_f, z_f, \varepsilon\right) = c_1 \int_{-\infty}^{\infty} p(\alpha) e^{-jk\left[\frac{y^{'}}{z_f} - \left(\frac{1}{z_f} r^2 + r\right)\varepsilon\right]\alpha} d\alpha$$

$$= c_1 \mathscr{F}\left[p(\alpha)\right]_{f_y = \frac{ry^{'}}{\lambda z_f} - \frac{r}{\lambda}\left(\frac{1}{z_f} r + 1\right)\varepsilon} \tag{9}$$

where $c_1 = e^{j\frac{k}{2}\left(r\varepsilon^2 + \frac{(y - r\varepsilon)^2 - y_f^2}{z_f}\right)}$. Eq. (9) represents the synthesized transmit beam pattern under the presence of randomized SAD ε, which turns out to be the Fourier transform of $p(\alpha)$ with corresponding frequency variable $f_y = \frac{ry^{'}}{\lambda z_f} - \frac{r}{\lambda}\left(\frac{1}{z_f} r + 1\right)\varepsilon$. This term indicates disorientation of the resultant beam, which is proportional to the ε with a configuration factor, which causes structural distortion in volumetric image reconstruction. Note that the individual transmit beam pattern would remain unchanged regardless of the presence of SAD. The SAD would only affect the scanning angle of the synthesized beam pattern as derived by Equation (9) in the radial direction.

2.4. Practical TRUS-rSAF implementation

In the given theoretical model, a fixed-lens elevation focusing of a TRUS array transducer should be further considered when defining a radial synthetic window. We here implement the TRUS-rSAF technique with the well-known approach of synthesizing wavefronts diverging from virtual sources (VSs) at a fixed lens focusing point for each transmittance/reception event (Fig. 3)[16], already established in our previous study [12]. We indicate the distances from the TRUS transducer to vS and vS to (y_f, z_f) as $d_{t1}(i, z)$ and $d_{t2}(i, z)$ at the i th dataset within a synthetic radial aperture window and z th focusing depth, respectively, whose sum comprises the total transmittance pathway $d_t(i, z)$, eventually defining transmit time-of-flight, $\tau_t(i, z) = d_t(i, z)/c$, where c is a speed of sound in biological tissue (i.e., 1540 m/sec). A reception distance d_r is defined by the shortest pathway between (y_f, z_f) and the current element position of the TRUS transducer (y_0, z_0). Receive time-of-flight $\tau_r(z) = d_r(z)/c$. In sum, a synthetic focusing delay at the scanning angle becomes $\tau_f(i, z) = \tau_t(i, z) + \tau_r(z)$.

In the TRUS-rSAF technique, a coherent synthesis of multiple transmittance/reception events can be equated by

$$S_{rSAF}(\theta_n, z) = \sum_{i = n - N_{syn}(z)/2}^{n + N_{syn}(z)/2} \overline{I}_i(\theta_n, z) \tag{10}$$

where θ_n and z are radial angle and depth of a target focus; $S_{\mathrm{rSAF}}(\theta_n, z)$ is a synthesized US intensity at the target; $N_{\mathrm{syn}}(z)$ is the radial synthetic

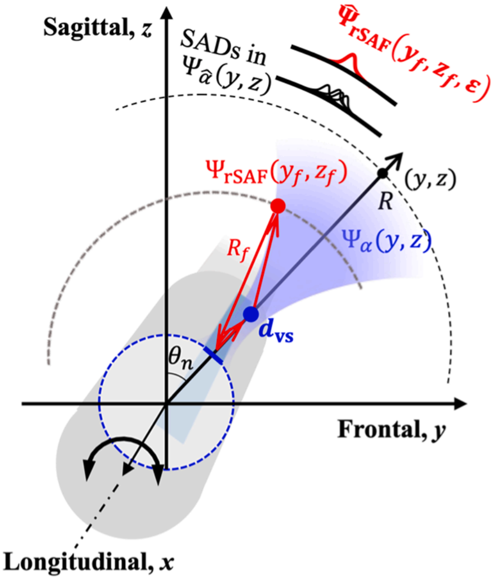

Fig. 3. Practical implementation of the TRUS-rSAF technique using virtual source (VS) scheme. Red dot indicates the beamforming pixel. At the target pixel, focusing delay-compensated acoustic beam will be superimposed with radial positioning error due to SAD, and the TRUS-rSAF technique will regulate the spatial fluctuation. Blue shaded region indicates the effective transmit beam field Ψ_α that defines radial synthetic window at each depth. (For interpretation of the references to colour in this figure legend, the reader is referred to the web version of this article.)

window at specific z; and $\overline{I}_i(\theta_n, z)$ is the US intensity from ith dataset within synthetic window (i.e., $I_i(\theta_n, z)$) which is delay-compensated by $\tau_f(i, z)$ for the target pixel $S_{\mathrm{rSAF}}(\theta_n, z)$. The model will be valid for each θ_n ($n = 1, 2, \ldots, N$), comprising the entire imaging volume. The important premise is that each beam profile in multiple transmittance/reception events should be included in the radial synthetic window defined by $N_{\mathrm{syn}}(z)$ pre-calibrated. We defined the radial synthetic window by a focusing geometry [17]. The reflection of SAD changes Eq. (10) into

$$\widehat{S}_{rSAF}(\theta_n, z, \varepsilon) = \sum_{i=n-N_{syn}(z)/2}^{n+N_{syn}(z)/2} \overline{I}_i(\theta_n + \varepsilon, z) \tag{11}$$

We assume ε to be in a normal distribution with zero mean and independent among individual radial scanning angles.

For a comparative evaluation, we simply define the TRUS-CON technique with $N_{\mathrm{syn}}(z)$ fixed at one throughout imaging depth, leading to $i = n$.

$$\widehat{S}_{\mathrm{CON}}(\theta_n, z, \varepsilon) = I_n(\theta_n + \varepsilon, z) \tag{12}$$

2.5. *Central limit theorem as a regulation mechanism for SAD*

We hypothesized that the TRUS-rSAF technique would alleviate the SAD by averaging multiple transmittance/reception events, as the projected imaging angle will be

$$E[\theta_n + \boldsymbol{\varepsilon}] \cong \theta_n \tag{13}$$

where $\boldsymbol{\varepsilon} = [\varepsilon_1, \varepsilon_2, \cdots, \varepsilon_{N_{\mathrm{syn}}}]$. It implies that more synthesis of adjacent radial planes will provide higher robustness to the uncertain radial SAD for volumetric TRUS imaging. The fundamental mechanism of the TRUS-rSAF technique follows the well-known Central Limit Theorem. With any distribution profile of the SAD with a standard deviation of σ, the resultant standard deviation of the mean scanning angles by the TRUS-rSAF technique, σ_{rSAF}, would be approximated by

$$\sigma_{\mathrm{rSAF}} = \frac{\sigma}{\sqrt{N_{\mathrm{syn}}}} \tag{14}$$

Therefore, the TRUS-rSAF technique will regulate the radial plane position with a narrower distribution over the target angle θ_n. Moreover, we include a frame averaging scheme as an additional SAD-alleviating mechanism for better structural preservation. In our case, Eq. (14) will be modified to reflect the distribution of SAD by

$$\sigma_{\mathrm{avg}} = \frac{\sigma_{\mathrm{rSAF}}}{\sqrt{N_{\mathrm{avg}}}} = \frac{\sigma}{\sqrt{N_{\mathrm{syn}} \bullet N_{\mathrm{avg}\bullet}}} \tag{15}$$

where N_{avg} is the number of frame averaging at each scanning angle. Here it should be noticed that such a mechanism based on the Central Limit Theorem is to statistically keep the center of the scanning angle distributions aligned with a target scanning angle rather than narrowing their distribution. The probability of a radial plane being within the radial synthetic window would still depend on the degree of SADs defined by σ, $N_{\mathrm{syn}}(z)$ and $\Delta\theta$. Detailed analysis will be in the Results section.

3. Quantitative evaluation

3.1. *Spatial expectation of synthetic beam profile*

Suppose the probability density function (PDF) of the random variable ε (i.e., $f(\varepsilon)$) is a normal distribution with zero mean ($\mu = 0$) with a standard deviation σ. The PDF can be equated by the Gaussian function as follows:

$$f(\varepsilon) = \frac{1}{\sigma\sqrt{2\pi}} e^{-\frac{\varepsilon^2}{2\sigma^2}} \tag{16}$$

From the given error model, the spatial expectation of the resultant synthetic beam pattern of the TRUS-rSAF technique (i.e., $E[\widehat{\Psi}_{rSAF}(y_f, z_f, \varepsilon)]$) can be formulated by

$$E[\widehat{\Psi}_{rSAF}(y_f, z_f, \varepsilon)] = \int_{-\infty}^{\infty} \widehat{\Psi}_{rSAF}(y_f, z_f, \varepsilon) f(\varepsilon) d\varepsilon$$

$$= \frac{1}{\sigma\sqrt{2\pi}} c_2 e^{\frac{q_2^2}{4q_1} - q_3} \sqrt{\frac{\pi}{q_1}\left(1 - e^{-\frac{q_1}{4}\alpha_{\mathrm{max}}^2}\right)} \tag{17}$$

where $q_1 = \frac{k^2\sigma^2 r^2 (z_f + r)^2}{2z_f[z_f - jk\sigma^2(z_f + r)r]}$, $q_2 = j\frac{k}{z_f}y' - \frac{k^2\sigma^2 r^2 (z_f + r)y}{z_f[z_f - jk\sigma^2(z_f + r)r]}$, and $q_3 = j\frac{k}{2z_f}(y^2 - y_f^2) - \frac{k^2\sigma^2 r^2 y^2}{2z_f[z_f - jk\sigma^2(z_f + r)r]}$. Eq. (17) defines the spatial probability of the $\widehat{\Psi}_{rSAF}(y_f, z_f, \varepsilon)$ in the frontal-sagittal domain as a function of the ε in a normal distribution. For example, one might consider an extreme case having $(y_f, z_f) = (0, 1)$, $r = 1$, $\theta_{\mathrm{max}} = 60^{\circ}$. Then, the resultant expectation of $\widehat{\Psi}_{rSAF}(0, 1, \varepsilon)$ can be simplified to

$$E[\widehat{\Psi}_{rSAF}(0, 1, \varepsilon)] \cong \sqrt{(1 - e^{-jk})e^{-\left(\frac{1}{4\sigma^2} - \frac{1}{2}jk\right)y^2}} \tag{18}$$

Eq. (18) shows that the range of expected SAD is inversely proportional to σ, which implies that a broad probability profile of the SAD may be more likely to have a severe radial shift of the synthesized beam profile.

We evaluate Eq. (17) under a clinical scenario using conventional specifications of a clinical TRUS imaging transducer (BPL9-5/55, BK Ultrasound, Inc., MA, USA): center frequency (f_c), 6.5 MHz; transducer radius r, 10 mm; elevation aperture size h, 5 mm; elevation focal point d_{vs}, 20 mm; radial FOV (θ_{FOV}), [-59.9948°, 59.9948°]; rotation interval $\Delta\theta$, 0.4724°; the number of radial scanning for a volume scanning event, 256. A range of SAD is assumed: $\sigma = \{0.1, 0.2, 0.5, 1.0, 2.0, 5.0\}^{\circ}$. The speed of sound ($c$) was fixed to 1540 m/s. The analysis of the beam profile was performed at two different focal points $(y_f, z_f) = $ (0 mm, 30 mm) and (0 mm, 60 mm).

3.2. *Field-II beam field simulation*

The Field-II beam field simulation validated the numerical estimation under identical imaging specifications. Fig. 4 shows the flowchart for iterative evaluation. From the specifications, a scanning angle for nth transmission is represented by.

$$\theta_n = -59.9948^{\circ} + (n-1)\cdot\Delta\theta,\ \text{where}\ n = 1, 2, 3, \cdots, 255 \tag{19}$$

Afterward, a synthetic beam profile at each depth z was composed by spatial compounding of adjacent $N_{syn}(z)$ radial planes. The dataset was prepared 16-times finer than the scanning angle interval (4,095 radial planes in θ_{FOV} [-59.9948°, 59.9948°]), and the SAD was reflected by randomly selecting a radial plane from them. The setup yielded the radial resolution up to $\Delta\theta_{\mathrm{FOV}} = \Delta\theta/16$ (i.e., 0.0295°), enabling finely quantized SADs. A range of SAD defined in the previous subsection was used for a direct comparison: $\sigma = \{0.1, 0.2, 0.5, 1.0, 2.0, 5.0\}^{\circ}$.

Once the images were reconstructed with 100-times permutations ($M = 100$), the peak radial position at each imaging depth was counted to compose a PDF plot. The TRUS-CON and TRUS-rSAF techniques reflected the SAD by selecting radial planes with the modified Eq. (19): $\widehat{\theta}_n = \theta_n + \widehat{\varepsilon}$. For comparison, the TRUS-CON and TRUS-rSAF images without the SAD were reconstructed as the ground-truths (TRUS-CON-GT and TRUS-rSAF-GT).

3.3. *Characterization of imaging performance and robustness*

Following the theoretical validation, the practical imaging performance was evaluated with different degrees of SADs. The simulation

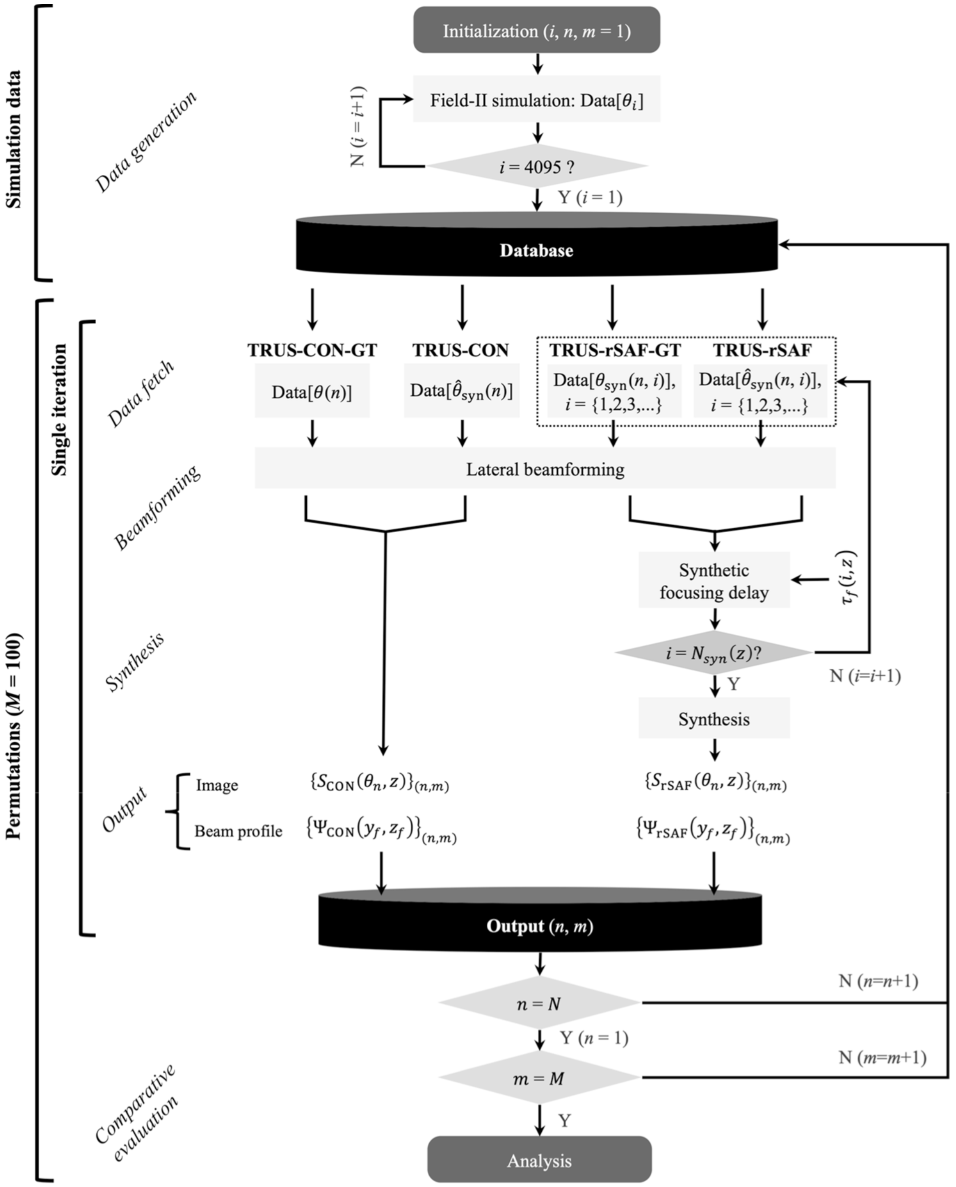

Fig. 4. Simulation framework. Abbreviations: a conventional TRUS technique with SADs, TRUS-CON; the TRUS-rSAF technique with SADs, TRUS-rSAF; current permutation index, m; current scanning index, n; a total number of radial scanlines in a frame, N; a total number of permutations, M; the SAD in a normal distribution, ε.

study characterized how much anatomical structure could be preserved compared to the TRUS-CON technique under the presence of the SADs. The data was again generated to provide the quantized SAD resolution 16-times higher than the scanning interval (i.e., 0.0295°). The database was used for all the comparison groups. For the selected radial plane, lateral beamforming was first performed using the transducer specifications. The radial TRUS images in the frontal-sagittal plane with and without SADs were considered for comparative evaluation (TRUS-CON & -rSAF vs TRUS-CON-GT & -rSAF-GT). The SAD-reflected groups were permutated 100 times ($M = 100$) for statistical evaluation.

The investigations were conducted from two points of view: (1) we first investigated the spatial resolution and statistical consistency to differentiate adjacent point targets. Two-point targets were positioned at each target depth from 30 mm to 70 mm in the 10-mm interval. The radial distance between adjacent targets at each depth was designed to be about two times of full-width-half-maximums (FWHMs) at the corresponding depths: {2.6, 2.9, 3.2, 4.5, 4.8} mm at {30, 40, 50, 60, 70} mm, respectively. (2) Also, the ability to preserve the structural features of a prostate-mimicking phantom simulation (Fig. 5) was also conducted in comparison to the ground-truth (GT) images as performance benchmarks (TRUS-CON-GT and TRUS-rSAF-GT). Wire targets possess a single pixel in the simulation grid, whose diameter is 59.23 μm, determined by the sampling frequency (i.e., 26 MHz = 4 f_c). Structure-similarity (SSIM) index was used to evaluate the preservation of overall structures, which is given by

$$SSIM(I,\widehat{I}) = \frac{(2\mu_I\mu_{\widehat{I}} + P_1)(2\sigma_{I\widehat{I}} + P_2)}{(\mu_I^2 + \mu_{\widehat{I}}^2 + P_1)(\sigma_I^2 + \sigma_{\widehat{I}}^2 + P_2)} \tag{20}$$

where I and $\widehat{I}$ indicate ground-truth and target images, μ and σ are the local mean and standard deviation of an individual image, and $P_1 = (0.01L)^2$ and $P_2 = (0.03L)^2$ with the specified dynamic range value of the image (L) [18]. In this evaluation, a more practical strategy, applying a frame averaging scheme ($N_{avg} = \{1, 5, 10, 15, 20, 30, 50, 80, 100\}$), was also evaluated, which will also suppress the SAD. The tradeoff between performance stabilization and loss in frame rate will be

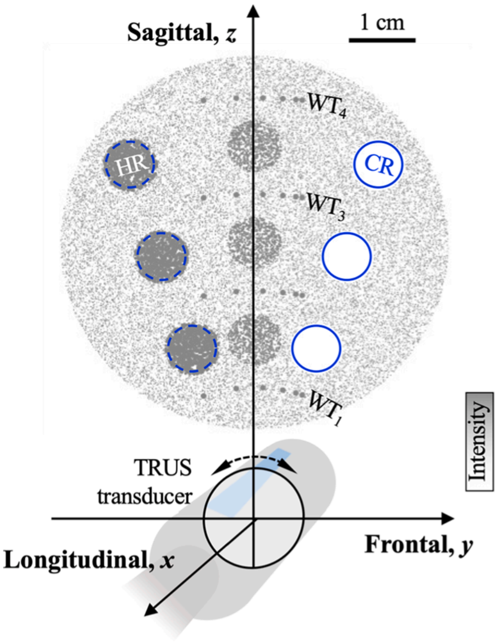

Fig. 5. Prostate-mimicking simulation setup. Abbreviation: wire targets, WT; hyperechoic region, HR; hypoechoic cyst region, CR. Black bar indicate 1-cm length.

thoroughly discussed.

3.4. Pelvic phantom experiment and performance evaluation

We have performed a tissue-mimicking phantom experiment using a clinically available TRUS transducer (BPL9-5/55, BK Medical, MA, USA) connected to a US research package (Vantage 256, Verasonics Inc., CA, USA). Radial scanning was performed by using a rotational stage (PRM1Z8, Thorlabs, Inc., NJ, USA) over θ_{FOV} of [-30.0°, 30.0°]) in the 0.0295° interval. A commercial tissue-mimicking multi-modal pelvic phantom (Model 048A, CIRS, VA, USA) was used for realistic performance evaluation. The transverse cross-section was selected to include prostate and hypoechoic urethral regions. The SSIM was first measured over the entire imaging FOV to be directly correlated to the simulation results. Also, contrast-to-noise ratio (*CNR*) was calculated to quantify the operator's perception of imaging quality, which is given by

$$CNR = \frac{|\mu_{\mathrm{t}} - \mu_{\mathrm{u}}|}{\sqrt{\sigma_{\mathrm{t}}^2 + \sigma_{\mathrm{u}}^2}} \tag{21}$$

where μ_t and μ_u indicate the mean US intensities and σ_t and σ_u represent the standard deviations in the prostate tissue and hypoechoic urethera regions, respectively.

4. Results

4.1. Define TRUS-rSAF parameters for clinical TRUS transducer

We first configured the TRUS-rSAF-GT technique for a TRUS transducer with the clinical specifications. From the volumetric US data with 120° of FOV and 255 radial planes, the $N_{\mathrm{syn}}(z)$ was determined among odd numbers (i.e., 1, 3, 5, 7, …) to secure the narrowest synthetic beam profile. Fig. 6a represents the mean FWHMs over imaging depth when the maximal $N_{\mathrm{syn}}(z)$ over the depth (i.e., $\widehat{N}_{\mathrm{syn}}$) are {3, 7, 15, 31}, in comparison to those by the TRUS-CON-GT technique (i.e., $\widehat{N}_{\mathrm{syn}} = 1$ throughout the imaging depth). The simulation produced the highest performance when seven radial planes were synthesized, but there was no noticeable enhancement in spatial resolution over the TRUS-CON-GT technique. One may question why an extended radial synthetic window does not lead to a tighter focusing, as given in a simple calculation yielding radial synthetic aperture width of 7.5 mm when $\widehat{N}_{\mathrm{syn}} = 31$, much broader than the original element height at 5 mm (50 % increase). However, we must remember the vital premise of having all the participating radial planes within the radial synthetic window. In this regard, the fixed-lens elevation focusing of the clinical TRUS transducer is a dominant factor limiting beam divergence and the width of the radial synthetic window. Fig. 6b shows the overlay of two outermost beam profiles when $\widehat{N}_{\mathrm{syn}} = \{3, 7, 15, 31\}$. Their scanning angles are at ± 0.4724°, ±1.4172 °, ±3.3068°, and ± 7.0860°, respectively. Fig. 6c shows the magnified profiles at 50-mm depth to present apparent

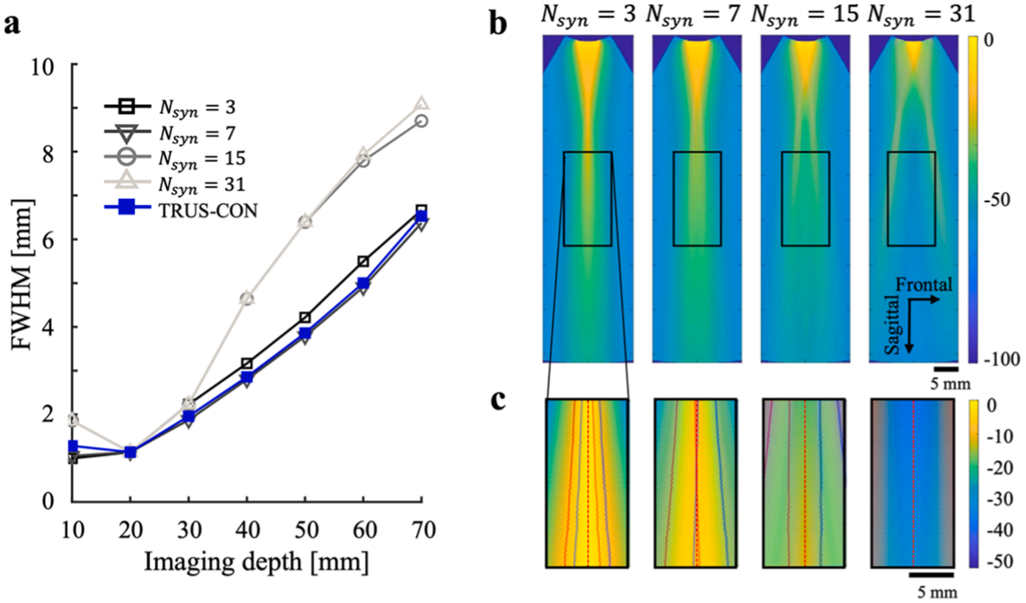

Fig. 6. Optimization of TRUS-rSAF technique. (a) Comparison in FWHM. **(b)** Overlay of the outermost beam fields. **(c)** −6-dB contours of the outmost beam profiles in magnified ROIs. The Blue and red lines indicate the rightmost and leftmost beams. Red dotted lines indicate the target synthetic scanline angle. (For interpretation of the references to colour in this figure legend, the reader is referred to the web version of this article.)

differences among them, where the red dotted line indicates a target angle θ_n, and solid lines indicate −6-dB contours of the beam profiles of the outmost planes. In the case of using $\widehat{N}_{\text{syn}} = 3$ and 7, the outermost beams successfully overlaid over the θ_n, while they went off when the wider window is applied (i.e., $\widehat{N}_{\text{syn}} = 15$ and 31). The effective radial aperture extension with $\widehat{N}_{\text{syn}} = 3$ and 7 are only 4 % and 12 % from the original element height, which justifies the results in Fig. 6a. We will keep applying this optimized setup (i.e., $\widehat{N}_{\text{syn}} = 7$) in the rest of the studies using the clinical TRUS transducer.

4.2. *Spatial probability distribution function under SAD*

This section characterizes the SAD effect on the TRUS-rSAF and TRUS-CON techniques using Field-II beam field analysis and further compared with the numerical analysis in the Eq. (17). From the permutated Field-II simulation ($M = 100$) under the exact transducer/imaging specifications, a peak radial position at each depth was counted in a spatial probability distribution plot (Fig. 7a). In this study, a high and narrow distribution centered at 0° would be preferred. The TRUS-rSAF technique yielded significantly higher peak probabilities averaged over the imaging depths than those by the TRUS-CON technique: {28.97 ± 5.77, 36.11 ± 18.78, 48.78 ± 9.64, 23.53 ± 60.64, 30.77 ± 20.24, 42.86 ± 37.64}-% increases when the SAD is with σ at {0.1, 0.2, 0.5, 1.0, 2.0, 5.0}°, respectively. In visual assessment, the width of the spatial probability distribution was progressively widened as a broader SAD was applied. On the theoretical side, Fig. 7b confirms the observation with the normalized theoretical expectation expressed in the Eq. (20), being proportional to σ given.

For further quantitative evaluation, mean spatial probability widths were measured from the Field-II simulation (Fig. 7c). The TRUS-rSAF technique consistently presented narrower widths than those derived by the TRUS-CON technique. The dotted black line indicates the statistical expectation of $\pm\sigma$, in which the trend is well-matched with that of the TRUS-CON technique. Otherwise, the TRUS-rSAF technique significantly reduced the spatial probability width. The ratio of spatial distribution width of the TRUS-rSAF over the TRUS-CON techniques were {71.43, 75.27, 59.89, 62.48, 55.62, 68.78} % when σ = {0.1, 0.2, 0.5, 1.0, 2.0, 5.0}°, respectively.

Fig. 7d presents the correlation between the widths of the spatial probability distribution functions in the Field-II simulation and the theoretical model in the Eq. (17). Each number is the average over imaging depths from 30 mm to 70 mm. Clear linear correlation was identified, validating the Field-II simulation results: slope at 1.11; y-intercept at −0.10°; and goodness of fit R^2 at 0.99. The coherent results from theory and simulation confirm the enhanced robustness against the SAD due to the TRUS-rSAF technique.

4.3. *Performance characterization in clinical TRUS transducer*

4.3.1. *Robustness against SAD*

Fig. 8a shows the radial TRUS images of wire targets reconstructed by the TRUS-rSAF and –CON techniques in frontal-sagittal (y-z) plane for the targets at 30-mm and 60-mm depths when σ = {0.1, 0.2, 0.5, 1.0, 2.0, 5.0}°. Note that TRUS-CON-GT and TRUS-rSAF-GT images were used as performance benchmarks. In visual assessment, the SADs produced structural distortion in wire targets in the TRUS-CON images, proportional to σ. In contrast, the TRUS-rSAF technique visually shows better robustness to SAD. Fig. 8b shows the radial intensity profiles when the SADs are presented, normalized by the corresponding maximal intensities in the TRUS-CON-GT profiles. Shaded regions in blue and gray indicate the standard deviations in the TRUS-rSAF and TRUS-CON techniques with the permutations of SAD 100 times. The averaged trends well agreed with those presented in the theoretical model and field analysis, being more distorted as σ increases in both techniques. One might notice that the reconstructed intensity of the TRUS-rSAF technique is slightly lower than the TRUS-CON technique. It is due to its synthesis of radial planes within the synthetic radial aperture window with a transmit acoustic power proportionally graded as being far from the center plane. It becomes apparent in a deeper imaging depth because of a widened radial synthetic window. However, our previous study showed that the signal-to-noise ratio (SNR) will still be higher in the TRUS-rSAF technique because of the lowered background noise level

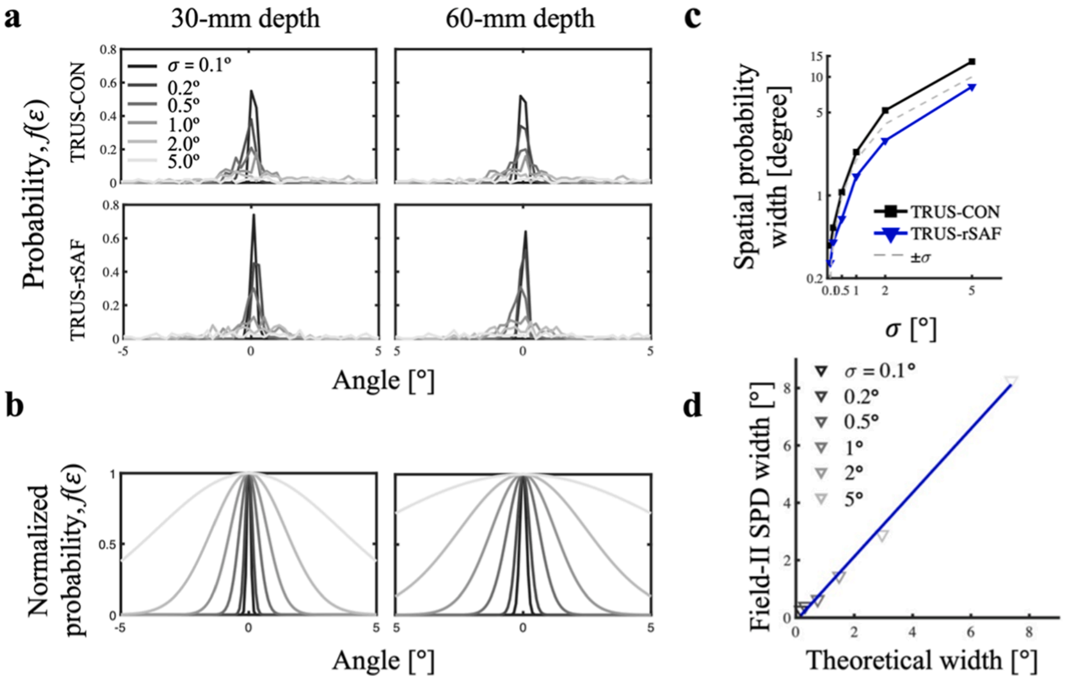

Fig. 7. Analysis of acoustic beam field. (a) Spatial probability distribution of peak profile positions at the depths-of-interest (i.e., 30 and 60 mm) with a presence of various SADs: σ = {0.1, 0.2, 0.5, 1.0, 2.0, 5.0}°. **(b)** Theoretical analysis. **(c)** The spatial probability distribution width. Dotted line indicates the statistical expectation, $\pm\sigma$. **(d)** Direct correlation between the Field-II simulation and theoretical model.

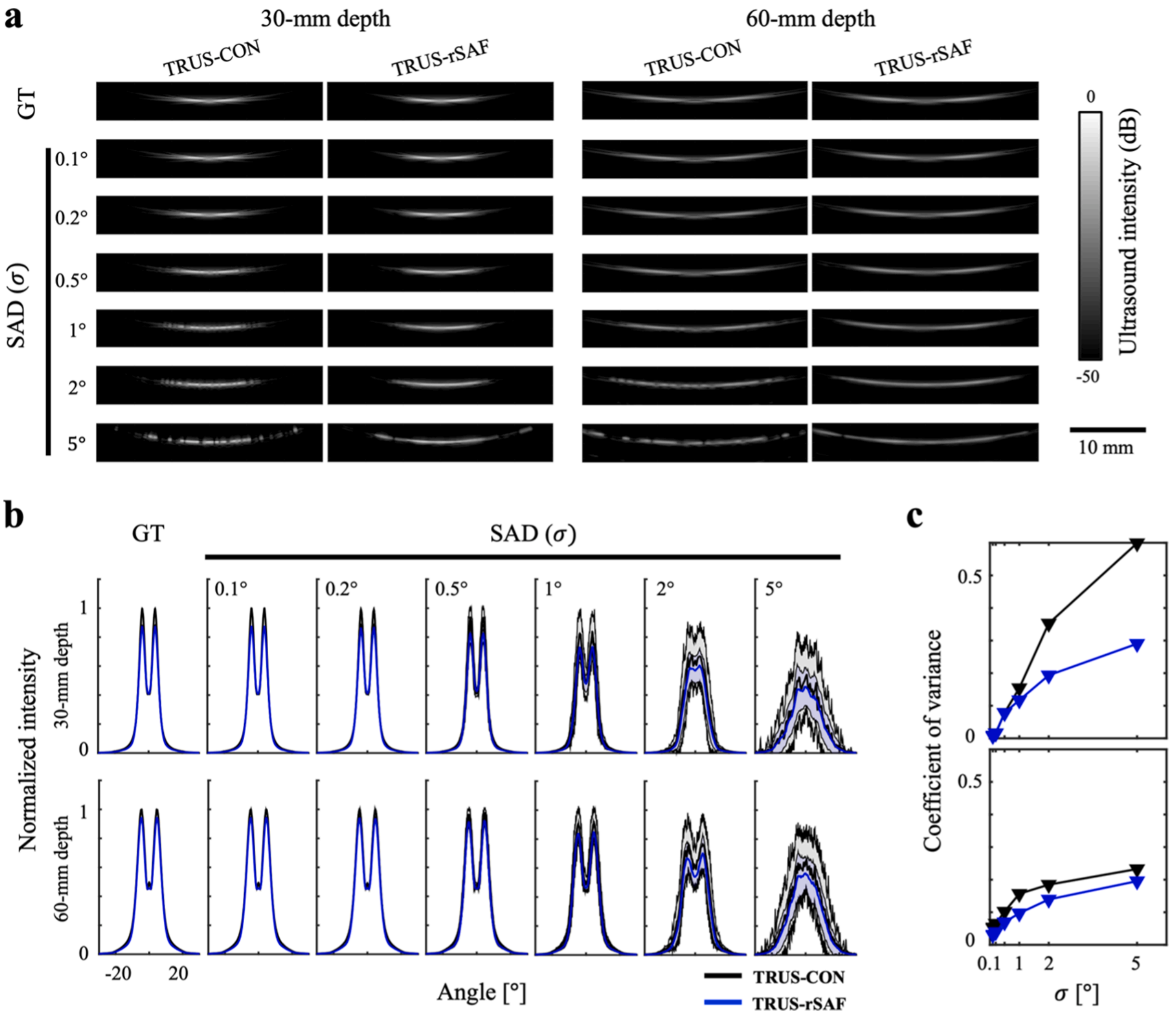

Fig. 8. Evaluation of two adjacent wire targets at 30-mm and 60-mm depths in the TRUS-CON and -rSAF techniques. (a) Wire target images with and without SADs. **(b)** Overlaid 1-D radial profiles taken from corresponding 2-D PSFs at (a). **(c)** The coefficients of variance.

[12]. In this paper, we focus on evaluating the robustness against SAD. Fig. 8c shows the coefficient of variance (CV) as a representative robustness metric. At 30-mm depth, the TRUS-rSAF and TRUS-CON techniques showed CVs of {0.01, 0.02, 0.08, 0.12, 0.20, 0.29} and {0.01, 0.02, 0.08, 0.15, 0.35, 0.60}, respectively at $\sigma = \{0.1, 0.2, 0.5, 1.0, 2.0, 5.0\}^\circ$. Also, at 60-mm depth, they provided CVs of {0.03, 0.04, 0.07, 0.10, 0.14, 0.20} and {0.05, 0.06, 0.10 0.16, 0.18, 0.24}, respectively. The fractional CV improvements of the TRUS-rSAF technique over the TRUS-CON technique were {2.68 %, 1.54 %, 0.01 %, 24.04 %, 45.11 %, 51.55 %} at 30-mm depth and {41.28 %, 39.43 %, 31.76 %, 38.06 %, 24.57 %, 15.95 %} at 60-mm depth when $\sigma = \{0.1, 0.2, 0.5, 1.0, 2.0, 5.0\}^\circ$, respectively. The results indicate that the TRUS-rSAF technique is more robust to the SAD than the TRUS-CON technique.

4.3.2. *Structural preservability*

Fig. 9a shows the TRUS images of a simulated prostate-mimicking phantom in the frontal-sagittal (y-z) plane, reconstructed by the TRUS-rSAF and TRUS-CON techniques with the range of SADs. In visual assessment, the TRUS-rSAF technique provided noticeable improvements in structural preservability compared to what was given by the TRUS-CON technique, agreeing with the theoretical model and simulation. We quantified the results by the SSIM metric. Fig. 9b shows the SSIM index plot of TRUS-rSAF and TRUS-CON techniques with respective references to the TRUS-rSAF-GT and TRUS-CON-GT techniques. Without frame averaging ($N_{\text{avg}} = 1$), the TRUS-rSAF technique presented SSIM indices of {0.98 ± 0.00, 0.96 ± 0.00, 0.88 ± 0.01, 0.74 ± 0.02, 0.53 ± 0.02, 0.32 ± 0.02} when $\sigma = \{0.1, 0.2, 0.5, 1.0, 2.0, 5.0\}^\circ$. On the other hand, the TRUS-CON technique yielded {0.95 ± 0.01, 0.92 ± 0.01, 0.84 ± 0.01, 0.72 ± 0.02, 0.56 ± 0.02, 0.37 ± 0.02}. The TRUS-rSAF technique shows significantly higher SSIMs than the TRUS-CON technique when $\sigma < 2.0^\circ$. However, the result was not improved when $\sigma \geq 2.0^\circ$. Remember that the TRUS-rSAF technique is effective only if the radial planes affected by the SAD are within the radial synthetic window. The probability of containing a transmit beam profile within the radial synthetic window can be estimated by the area-under-normal distribution at each σ. If assuming a radial synthetic window extending over $\pm 1.4172^\circ$ angle ($\widehat{N}_{\text{syn}} = 7$), the planes would be located at 0°, $\pm 0.4724^\circ$, $\pm 0.9448^\circ$, $\pm 1.4172^\circ$ (θ_n, $\theta_n \pm \Delta\theta$, $\theta_n \pm 2\,\Delta\theta$, and $\theta_n \pm 3\,\Delta\theta$). When considering the SADs with σ at $\{0.1, 0.2, 0.5, 1.0, 2.0, 5.0\}^\circ$, each radial planes will have the overlapped areas of {1.00, 1.00, 1.00, 0.84, 0.52, 0.22} at 0°, {1.00, 1.00, 0.97, 0.80, 0.51, 0.22} at $\pm$ 0.4724°, {1.00, 0.99, 0.83, 0.67, 0.47, 0.22} at $\pm$ 0.9448°, and {0.50, 0.50, 0.50, 0.50, 0.42, 0.21} at $\pm$ 1.4172°, respectively. Therefore, the projected probabilities to be within a radial synthetic window for 7 radial planes (P_a) would be {0.86, 0.85, 0.80, 0.68, 0.47, 0.22} for $\sigma = \{0.1, 0.2, 0.5, 1.0, 2.0, 5.0\}^\circ$. The trend explains the performance lower than expected when $\sigma > 2.0^\circ$, and well matches with the SSIM evaluation in Fig. 9b.

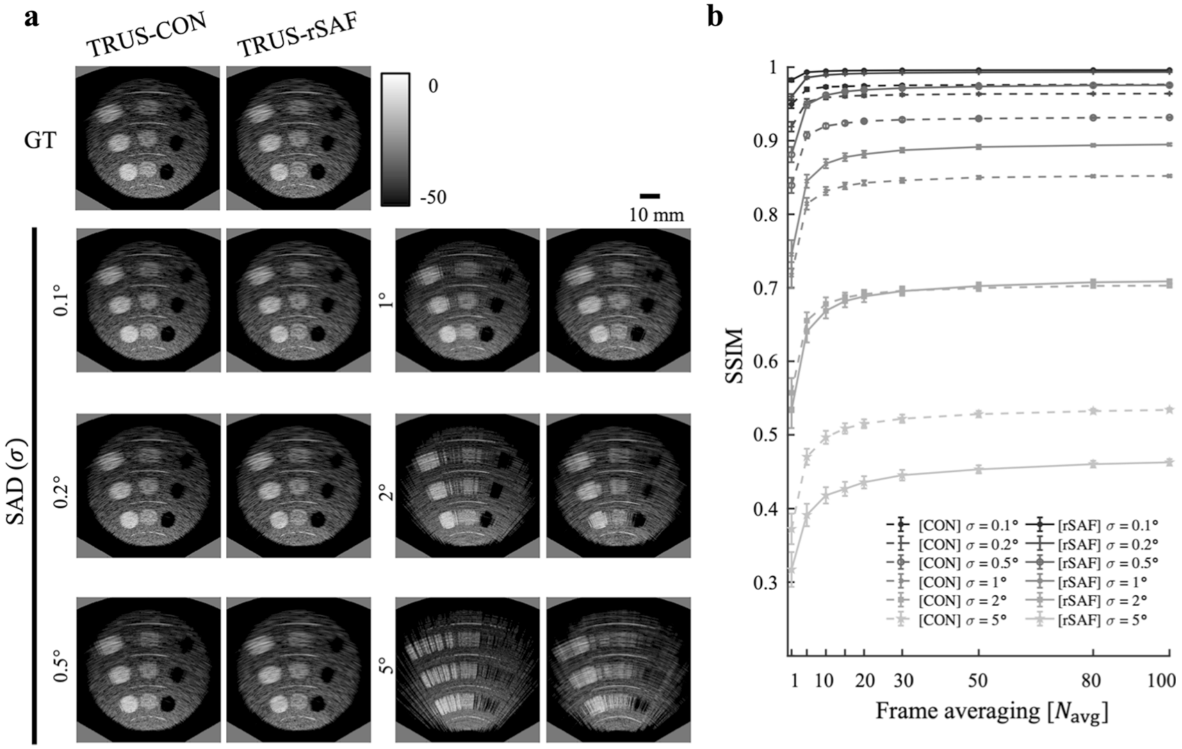

Fig. 9. Prostate-mimicking phantom imaging. (a) B-mode images. **(b)** Structure-similarity (SSIM) index ($M = 100$).

The correlation between P_α and SSIM values (without frame averaging) yield a high correlation with the slope of 1.028, the y-intercept of 0.07, and R^2 at 0.9912. Averaging 100 frames provided the SSIM values at {1.00 ± 0.00, 0.99 ± 0.00, 0.98 ± 0.00, 0.89 ± 0.00, 0.71 ± 0.00, 0.46 ± 0.00} for $\sigma = \{0.1, 0.2, 0.5, 1.0, 2.0, 5.0\}^\circ$. However, the improvements due to the frame averaging were still capped when a part of radial planes was out of the radial synthetic window. It should also be noted that the frame averaging scheme will lower the temporal resolution

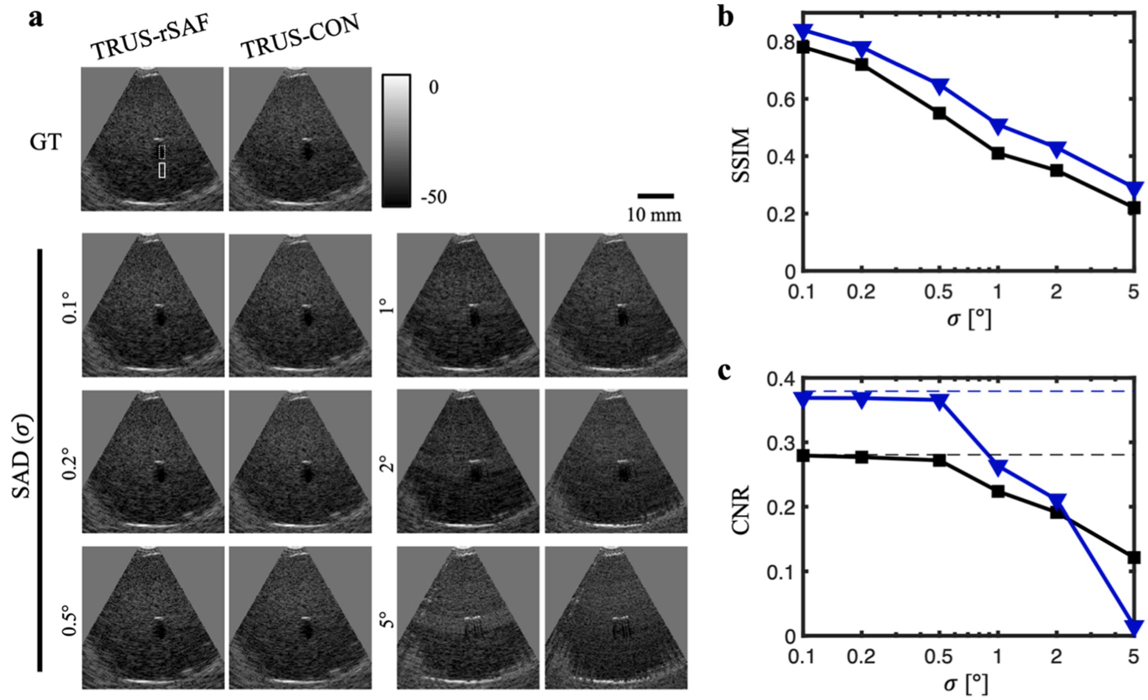

Fig. 10. Tissue-mimicking pelvic phantom experiment. (a) B-mode images. Solid and dotted rectangular indicators show the speckle and cyst regions for CNR calculation. **(b)** Structure-similarity (SSIM) index. **(c)** Contrast-to-noise ratio (CNR). Dotted blue and black lines indicate the CNR values measured from the GT datasets by the TRUS-rSAF and TRUS-CON techniques, respectively. (For interpretation of the references to colour in this figure legend, the reader is referred to the web version of this article.)

because it necessitates multiple transmittance/reception events at each scanning angle, while the TRUS-rSAF technique does not require any decrease in radial scanning speed.

4.3.3. Tissue-mimicking pelvic phantom evaluation

Fig. 10 shows the results of the tissue-mimicking phantom experiments. In visual assessment, the TRUS-rSAF technique delivered consistent outcomes as presented in simulation studies, securing higher robustness than the TRUS-CON technique when the SAD is well-contained within the radial synthetic window ($<\pm 1.4172^{\circ}$). Quantitative assessment was performed to evaluate the imaging performance. The measured SSIM values are {0.84, 0.78, 0.65, 0.51, 0.43, 0.29} for the TRUS-rSAF technique and {0.78, 0.72, 0.55, 0.41, 0.35, 0.22} for the TRUS-CON technique when $\sigma = \{0.1, 0.2, 0.5, 1.0, 2.0, 5.0\}^{\circ}$. The result shows 7.7–31.8 % higher SSIM values in the TRUS-rSAF techniques than the counterparts of the TRUS-CON technique.

However, additional analysis that represent a operator's perception of the image quality was needed. The CNR was calculated using the regions-of-interest indicated by the solid and dotted rectangular indicators in Fig. 10a. The CNR were {0.37, 0.37, 0.37, 0.26, 0.21, 0.01} for the TRUS-rSAF technique, and {0.28, 0.28, 0.27, 0.22, 0.19, 0.12} for the TRUS-CON technique when $\sigma = \{0.1, 0.2, 0.5, 1.0, 2.0, 5.0\}^{\circ}$, respectively. The CNR values in the GT datasets were 0.38 and 0.28 for the TRUS-rSAF and TRUS-CON techniques. It indicates that the TRUS-rSAF technique would provide the CNR comparable with the TRUS-CON technique when $\sigma < 1^{\circ}$. As increasing σ, CNR values in both techniques were progressively reduced. Notably, in the out of the radial synthetic window ($\sigma > 1.4172^{\circ}$), the CNR of the TRUS-rSAF technique became even lower than the TRUS-CON technique, which reminds its requirement to contain the SAD within the radial synthetic window. Therefore, the pelvic phantom experiment successfully validated the simulation outcomes.

4.4. Performance characterization with customized TRUS-rSAF transducer

The results from the above sections demonstrated the improved robustness of the TRUS-rSAF technique against the various degree of SADs compared to the TRUS-CON technique. However, there was no benefit in spatial resolution due to the limited size of the radial synthetic window (i.e., $\widehat{N}_{\text{syn}}$=7). Here we further explore how the broadness of the radial synthetic window affects the volumetric TRUS imaging in the presence of the SAD. The analytical solution of the TRUS-rSAF technique, which our group has recently established, provides a quantitative design framework to optimize spatial resolution and grating lobe positions [12], as presented in the Eq. (5). The theoretical description unveils that its spatial resolution is proportional to r and α_{max}. Our optimization considered clinical practicality with r to prevent pain during the insertion and imaging of the TRUS transducer: $r = 15$ mm. A conventional TRUS transducer has r around 10 mm. On the other hand, α_{max} is determined by the f-number, the ratio of focal depth (d_{vs}) and the active element aperture (h) – low f-number (shorter d_{vs} and wider h) result in a broader acoustic divergency that allows a wider radial synthetic window. Our optimization yielded h, and d_{vs} of 7 mm and 5 mm, respectively, which are different from those in a conventional TRUS transducer (h of 5 mm and d_{vs} of 20–25 mm). Radial scanning interval ($\Delta\alpha$) is also important to define the grating lobe artifacts. Finer radial scanning pushes granting lobe from a central radial plane, resulting in lower grating lobe artifacts. We selected the $\Delta\alpha$ of 0.2362° to provide negligible grating lobe artifacts but with a reasonable volume scanning rate (2–3 volumes per second). Herein, we name the optimized TRUS-rSAF technique as the TRUS-rSAF-OPT technique. Our optimization based on our analytical solution broadened the radial synthetic window up to $\widehat{N}_{\text{syn}} = 131$ at $\Delta\theta = 0.2362^{\circ}$ for negligible grating lobe artifacts, providing 36-% narrower FWHM over prostate imaging depth (30–70 mm). It gives a dramatic 10.93-times broadening of the radial synthetic window from 2.83° to 30.94°. In sum, we expected the TRUS-rSAF-OPT technique to concurrently secure a higher spatial resolution and SAD regulation. Fig. 11a visually presents the spatial resolution improvement without the SAD presence, comparing the ground-truth TRUS-rSAF-OPT (TRUS-rSAF-OPT-GT) technique with the TRUS-rSAF-GT and TRUS-CON-GT techniques that use a clinical TRUS transducer. The radial profiles again confirm the improvements (Fig. 11b). The TRUS-rSAF-GT technique using a clinical TRUS transducer did not present any benefit in enhancing spatial resolution over the TRUS-CON-GT technique, as already presented in Fig. 6.

Using the TRUS-rSAF-OPT technique, we tested the impact of the SADs on image quality (Fig. 12). In visual assessment, the TRUS-rSAF-OPT technique seems to provide better spatial resolution but revealed radial image artifacts from hyper-echoic mass targets located at near-depth regions even when $\sigma = 0.1^{\circ}$, and further deteriorated as σ increases (Fig. 12a,b). The wider radial synthetic window of the TRUS-rSAF-OPT technique fails to cancel the phases of sidelobes among the radial planes under the unpredictable SADs. Fig. 12c shows the corresponding SSIM assessment with the TRUS-rSAF-OPT-GT image for extended SAD range: {0.97 ± 0.00, 0.91 ± 0.01, 0.79 ± 0.01, 0.69 ± 0.01, 0.61 ± 0.01, 0.53 ± 0.01} for $\sigma = \{0.1, 0.2, 0.5, 1.0, 2.0, 5.0\}^{\circ}$. The SSIM values of the TRUS-rSAF-OPT technique were significantly lower than those of the conventional TRUS-rSAF technique. Therefore, despite potentially higher structural preservability and spatial resolution, the TRUS-rSAF-OPT technique may limit efficacy in practical clinics with low contrast resolution, suggesting its limited role in a premium TRUS imaging device. This result gives extended perspectives on the mutual relationship between the degree of radial synthesis and robustness to the SADs with a chained effect to produce the sidelobe artifacts. However, its impact on technology translation would be minimal because the customization of the TRUS transducer is not an option to secure cost-effectiveness for resource- and budget-limited circumstances.

5. Discussion

In this paper, we presented the TRUS-rSAF technique as a novel technological foundation to enable an economical form factor of the volumetric TRUS imaging in resource- and budget-limited clinics. Theoretical SAD modeling in the TRUS-rSAF technique was first established (Eqs. (6–9), Figs. 1-3), and its more robust SAD regulation compared to the TRUS-CON technique was validated through a strong agreement between the numerical model, field analysis (Figs. 6, 7), imaging simulations (Figs. 8, 9), and tissue-mimicking phantom experiment (Fig. 10). For example, one might recycle a non-motorized TRUS transducer retired from a hospital and give a second life in limited environments at a minimal cost. Modern US system technologies may support TRUS imaging at a minimal hardware cost by using an ultra-compact multi-channel US module [20–23] and a probe adaptor board. An embedded camera in a personal device can track radial scanning, and the TRUS-rSAF technique can regulate its low-resolution tracking error. It would be much more economical than adopting a 3-D TRUS imaging device that uses a fully motorized TRUS transducer controlled by dedicated hardware and software. To expand our perspectives, we further tested a hypothesis that TRUS imaging by an optimized TRUS transducer, providing an extended radial synthetic window, will secure concurrent improvements in spatial resolution and robustness to SADs (Figs. 11, 12). The study unveiled that a sidelobe level is another important parameter to provide clinically relevant image quality in the presence of SAD. However, it should be noted that complete customization of a TRUS transducer is not an option to maximize cost-effectiveness, and the implication of the study is limited in technological testing and evaluation.

Once the data is collected, the computational requirements for the TRUS-rSAF technique can be marginally handled in a modern personal

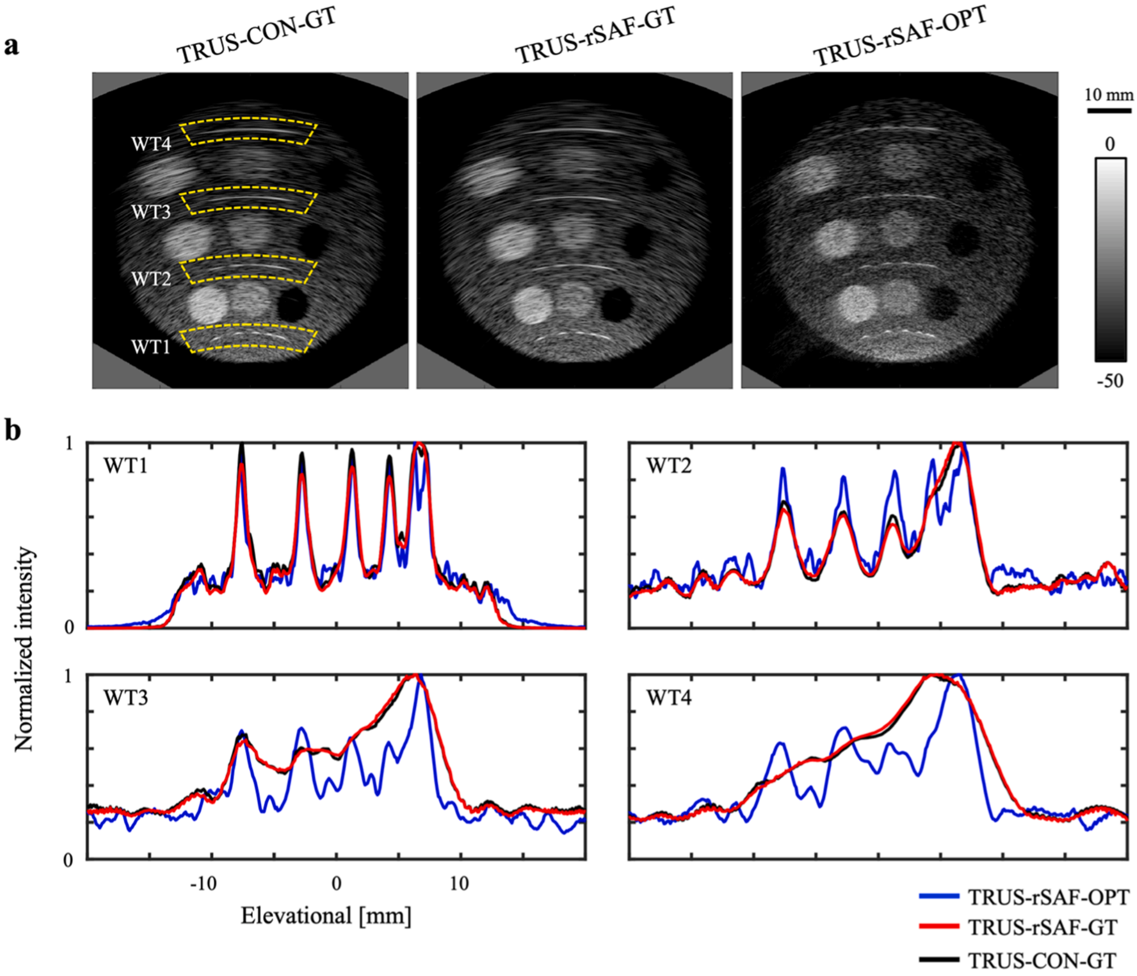

Fig. 11. Performance enhancement in the optimized TRUS-rSAF transducer. The reconstructed image of TRUS-rSAF-OPT technique in comparison to those by the TRUS-CON-GT and TRUS-rSAF-GT techniques. Radial profiles of the images were drawn for wire targets (WTs) at different depths.

device (e.g., laptop, tablet, or smartphone) that has enlarged its roles in the medical US imaging field [19–22]. To get a basic sense, a volumetric reconstruction by the TRUS-CON and TRUS-rSAF techniques took 12.4 and 18.5 h, respectively, using single-core software in the personal laptop (2.6 GHz Intel Core i7 8850H, 16 GB RAM, MATLAB 2020b). It does not represent practical performance but reflects a projected increase in computing time approximated by 49.2 % due to the TRUS-rSAF technique. A modern graphical processing unit (GPU)-based parallel processing and efficient beamforming architectures have enabled massive SAF techniques in the biomedical US imaging field [23–26]. Modern personal devices equipped with state-of-art GPU processors or cloud computing are now capable of dealing with real-time medical US imaging, demonstrated by several commercial products (e.g., Vscan by GE Ultrasound, Lumify by Philips Healthcare, Butterfly IQ by Butterfly Network, etc.). Therefore, no technological hurdle is anticipated to secure a clinically appropriate performance of the TRUS-rSAF technique in a personal device.

There are several further works towards translating the TRUS-rSAF technique into clinical practice in resource- and budget-limited settings. Our immediate task is to advance the theoretical foundation to reflect a more practical resource-limiting setting. We may alternate the SAD model from a simple normal distribution ($\widehat{\alpha}$ and $\widehat{\beta}$ in Eq. (6)) to a real-world measurement using external sensors for radial tracking. It will provide a more realistic evaluation of the TRUS-rSAF technique to alleviate the SAD-induced image distortions.

Based on the advanced theory, our translational task would focus on developing a prototype device with the most economical configuration using an ultra-compact US system with a clinical TRUS transducer and external tracker connected to a personal device for signal processing and image display. Recently there has been a noticeable trend democratizing US imaging systems with hand-held form factors and easy connectivity to personal devices, such as smartphones, tablets, and laptops, based on the rapid evolution of chip integration technologies, efficient architectures, and algorithms [19–21,27–31]. Multiple form factors could be embodied with our primary goal for cost-effectiveness, by which we exclude any motorized rotational actuator to minimize the system complexity and burden for additional calibration. We plan a self-contained solution using a multi-camera tracker implementable in modern mobile smart devices. Previous studies have presented object tracking algorithms using a monocular or stereo camera. For example, Liu *et al.* [33,34] and Prisacariu *et al.* [35] used pixel-wise posteriors 3D (PWP3D) algorithms to estimate the 3D position and orientations of a target with a monocular camera. The state-of-the-art PWP3D algorithm offers a mean estimation error from 1.61° to 15.68°, depending on the speed of the moving target, which should be minimized in the clinical scenario with slow scanning procedures and relatively stationary tissue movements. In addition, Wang *et al.* [36] used an RGB-D camera to estimate the 6-degree-of-freedom tracking of an object. Looking at the prior arts, we anticipate specific challenges from the limited tracking accuracy of the cameras in a mobile device and the requirement of real-time tracking and synchronization to the scanning sequences. However, such limitations will be alleviated as mobile computing technology evolves. Prisacariu *et al.* [37] recently proposed real-time 3-D tracking of an object using a GPU-driven mobile phone. By using the internal

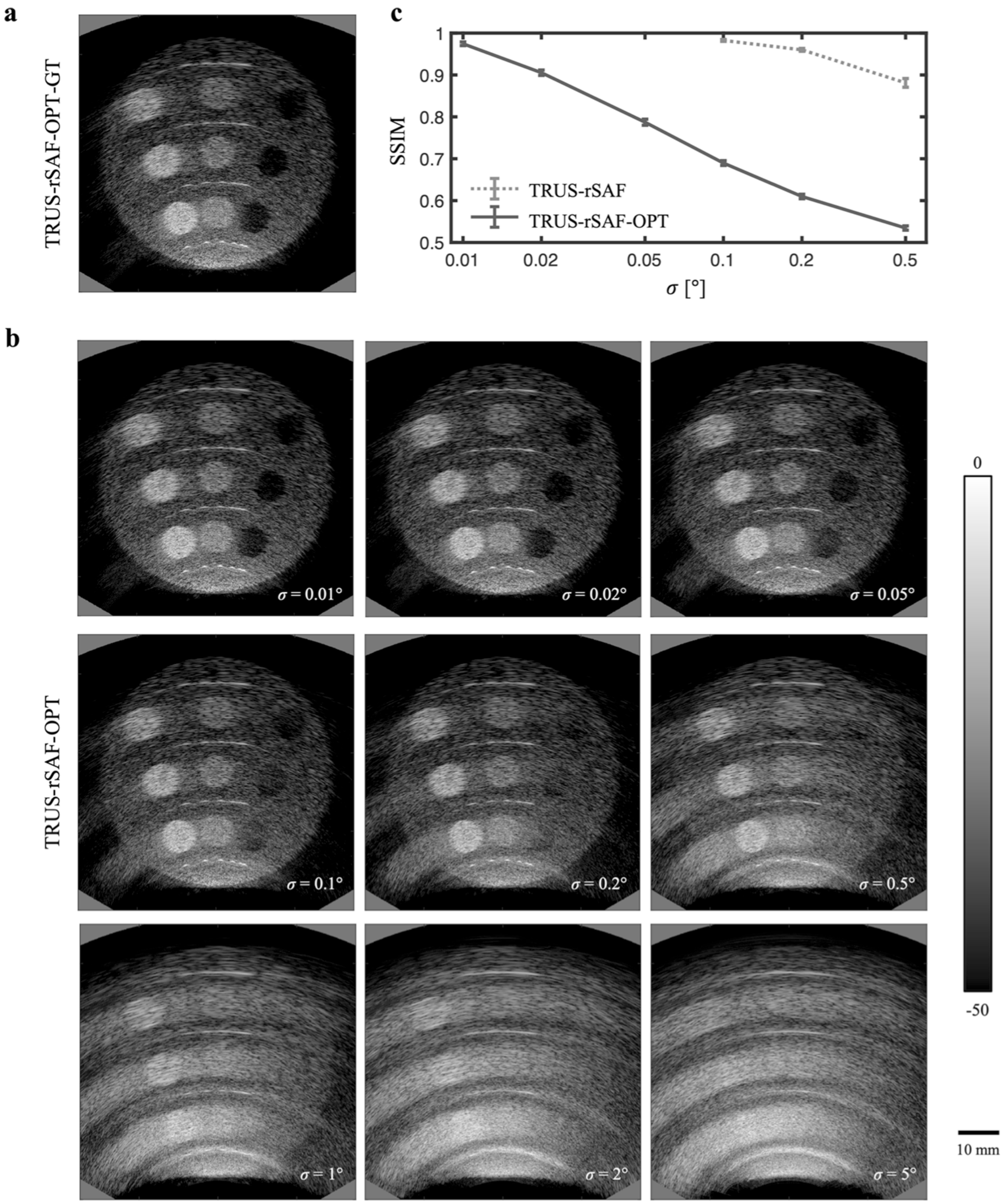

Fig. 12. Structural preservability test under a range of SADs. (a) A ground-truth TRUS-rSAF image without SAD. (b) The TRUS-rSAF images with a range of SAD. (c) SSIM values of the TRUS-rSAF images with clinical (TRUS-rSAF) and optimized TRUS transducers (TRUS-rSAF-OPT).

inertial sensor in a typical mobile phone, the algorithm achieves its rotation accuracy up to 1.3°, which falls into our performance goal. Also, it is reported that the tracking algorithm and frame registrations take 31 and 11.3 frames per second (fps) on an iPhone 5 s, respectively. A novel and faster solution can be developed to achieve higher temporal resolution.

Along with the hardware platform, there would also be an exciting direction to develop an effective and efficient clinical interface that allows clinicians to collect and navigate the volumetric data easier, also enabled by external tracking technologies [32,33]. In this developmental process, realistic SAD modeling would be an essential step to secure the necessary accuracy in the TRUS-rSAF technique, which depends on the tracking methodologies.

The clinical application of the TRUS-rSAF technique will not be limited to the morphological investigation by conventional TRUS imaging in clinics. Photoacoustic (PA) imaging is an emerging modality in science and clinics in which rich optical contrast can be obtained from biological tissue at sub-millimeter spatial resolution and centimeter-scale imaging depth [34,35]. The scientific and engineering innovations are rapidly expanding to clinical neurology and oncology [36–43]. In particular, we have successfully presented the feasibility of identifying prostate-specific membrane antigen (PSMA), enabling minimally-invasive differential diagnosis of aggressive cancer types over benign ones [39,44,45]. Our economical solution proposed here could also be a technological foundation to democratize molecular imaging for prostate cancer management in resource-limited settings.

6. Conclusion

In this study, we validated the TRUS-rSAF technique to regulate the SAD during manual volumetric scanning using a clinical TRUS imaging transducer. It may enable an economic TRUS imaging device to democratize the TRUS for pelvic inspection with minimal cost for healthcare providers and patients. We further characterized the competing effects of broader radial synthesis and side lobe artifacts in an individual radial plane. It indicated the importance of defining TRUS transducer specifications to minimize the side lobe, which is already achieved in clinical TRUS array transducers. The technical merits of the TRUS-rSAF technique do not bound to pelvic applications and can extend arbitrary imaging scenarios as long as it includes a radial scanning component or unpredictable subject movements in the radial plane.

Author contributions statement

JK conceived the research, directed the project, led the data analysis, and revised the manuscript. HS conducted the theoretical formulation, simulation, data processing & analysis and wrote the first manuscript. EB supervised the research activities and co-directed the research. All the authors confirmed the final manuscript.

Declaration of Competing Interest

The authors declare that they have no known competing financial interests or personal relationships that could have appeared to influence the work reported in this paper.

Data availability

Data will be made available on request.

Acknowledgments

This work was supported by the Congressionally Directed Medical Research Programs, U.S. Department of Defense (DOD), USA (W81XWH-18-1-0188), NIH National Cancer Institute (NCI), USA (R01CA134675), and NSF Career award (1653322).

References

[1] E.J. Trabulsi, D. Sackett, L.G. Gomella, E.J. Halpern, Enhanced transrectal ultrasound modalities in the diagnosis of prostate cancer, Urology 76 (2010) 1025–1033, https://doi.org/10.1016/j.urology.2010.05.022.

[2] P. Perrin, Transrectal ultrasound for the diagnosis and staging of prostate cancer, Curr. Opin. Urol. 2 (1992) 344–347, https://doi.org/10.1097/00042307-199210000-00005.

[3] A. Peltier, F. Aoun, F. El-Khoury, E. Hawaux, K. Limani, K. Narahari, N. Sirtaine, R. van Velthoven, 3D versus 2D systematic transrectal ultrasound-guided prostate biopsy: higher cancer detection rate in clinical practice, Prostate Cancer 2013 (2013) 1–5, https://doi.org/10.1155/2013/783243.

[4] X. Zhang, J. Fan, L. Zhang, J. Wang, M. Wang, J. Zhu, Association between three-dimensional transrectal ultrasound findings and tumor response to neoadjuvant chemoradiotherapy in locally advanced rectal cancer: an observational study, Front. Oncol. 11 (2021), 648839, https://doi.org/10.3389/fonc.2021.648839.

[5] A. Fenster, D.B. Downey, Three-dimensional ultrasound imaging, Annu. Rev. Biomed. Eng. 2 (2000) 457–475, https://doi.org/10.1146/annurev.bioeng.2.1.457.

[6] J.-F. Guo, Y.-L. Cai, Y.-P. Wang, Morphology-based interpolation for 3D medical image reconstruction, Comput. Med. Imag. Grap. 19 (1995) 267–279, https://doi.org/10.1016/0895-6111(95)00007-d.

[7] R.W. Parrott, M.R. Stytz, P. Amburn, D. Robinson, Towards statistically optimal interpolation for 3D medical imaging, Ieee Eng. Med. Biol. 12 (1993) 49–59, https://doi.org/10.1109/51.232341.

[8] M.-A. Janvier, L.-G. Durand, M.-H.-R. Cardinal, I. Renaud, B. Chayer, P. Bigras, J. de Guise, G. Soulez, G. Cloutier, Performance evaluation of a medical robotic 3D-ultrasound imaging system, Med. Image Anal. 12 (2008) 275–290, https://doi.org/10.1016/j.media.2007.10.006.

[9] S. Bae, P. Kim, T. Song, Ultrasonic sector imaging using plane wave synthetic focusing with a convex array transducer, J. Acoust. Soc. Am. 144 (2018) 2627–2644, https://doi.org/10.1121/1.5065391.

[10] J. Kortbek, J.A. Jensen, K.L. Gammelmark, Sequential beamforming for synthetic aperture imaging, Ultrasonics 53 (2013) 1–16, https://doi.org/10.1016/j.ultras.2012.06.006.

[11] J. Kortbek, Jã.A. Jensen, K.Lã. Gammelmark, Synthetic aperture focusing applied to imaging using a rotating single element transducer, 2007 Ieee Ultrasonics Symposium Proc. (2007) 1504–1507. https://doi.org/10.1109/ultsym.2007.378..

[12] H. Song, J. Kang, E.M. Boctor, A novel design framework of synthetic radial aperture focusing for volumetric transrectal ultrasound imaging, J Comput Des Eng. 9 (2022) 1852–1865. https://doi.org/10.1093/jcde/qwac083.

[13] J.A. Jensen, Field: A program for simulating ultrasound systems, (n.d.).

[14] J.A. Jensen, N.B. Svendsen, Calculation of pressure fields from arbitrarily shaped, apodized, and excited ultrasound transducers, Ieee Trans. Ultrason. Ferroelectr. Freq. Control. 39 (1992) 262–267, https://doi.org/10.1109/58.139123.

[15] Brilliant.org, Small-Angle Approximation, (n.d.). https://brilliant.org/wiki/small-angle-approximation/ (accessed 2022).

[16] C.H. Frazier, W.D.O. Jr, Synthetic aperture techniques with a virtual source element, Ieee Trans. Ultrason. Ferroelectr. Freq. Control. 45 (1998) 196–207, https://doi.org/10.1109/58.646925.

[17] K.-S. Kim, T.K. Song, High frame rate and high resolution imaging with synthetic aperture, Key Eng. Mat. 270–273 (2004) 168–173, https://doi.org/10.4028/www.scientific.net/kem.270-273.168.

[18] Z. Wang, E.P. Simoncelli, A.C. Bovik, Multiscale structural similarity for image quality assessment, (2007) 71–80. https://doi.org/10.1109/acssc.2003.1292216.

[19] Sewoong, Jeeun, Pilsu, Gunho, Eunji, Woojin, Minsuk, Tai-Kyong, Smartphone-Based Portable Ultrasound Imaging System: Prototype Implementation and Evaluation, in: 2015: pp. 1–4. https://doi.org/10.1109/ultsym.2015.0517..

[20] Y. Lee, J. Kang, S. Yeo, J. Lee, G.-D. Kim, Y. Yoo, T.-K. Song, A New Smart Probe System for a Tablet PC-Based Point-of-Care Ultrasound Imaging System: Feasibility Study, in: 2014: pp. 1611–1614. https://doi.org/10.1109/ultsym.2014.0399.

[21] E. Jeong, S. Bae, M. Park, W. Jung, J. Kang, T.-K. Song, Color Doppler Imaging on a Smartphone-Based Portable us System: Preliminary Study, in: 2015: pp. 1–4. https://doi.org/10.1109/ultsym.2015.0518.

[22] M. Park, J. Kang, G. Lee, M. Kim, T.-K. Song, A new post-phase rotation based dynamic receive beamforming architecture for smartphone-based wireless ultrasound imaging, Proc Spie. (2016) 97901V-97901V–6. https://doi.org/10.1117/12.2216705..

[23] J.-H. Park, C. Yoon, J.H. Chang, Y. Yoo, T.-K. Song, A Real-time Synthetic Aperture Beamformer for Medical Ultrasound Imaging, 2010 Ieee Int Ultrasonics Symposium. (2010) 1992–1995. https://doi.org/10.1109/ultsym.2010.5935734..

[24] B.Y.S. Yiu, I.K.H. Tsang, A.C.H. Yu, GPU-based beamformer: fast realization of plane wave compounding and synthetic aperture imaging, Ieee Trans. Ultrason. Ferroelectr. Freq. Control. 58 (2011) 1698–1705, https://doi.org/10.1109/tuffc.2011.1999.

[25] M.B. Stuart, P.M. Jensen, J.T.R. Olsen, A.B. Kristensen, M. Schou, B. Dammann, H. H.B. Sørensen, J.A. Jensen, Real-time volumetric synthetic aperture software beamforming of row-column probe data, Ieee Trans. Ultrason. Ferroelectr. Freq. Control. 68 (2021) 2608–2618, https://doi.org/10.1109/tuffc.2021.3071810.

[26] J.A. Jensen, H. Holten-Lund, R.T. Nilsson, M. Hansen, U.D. Larsen, R.P. Domsten, B.G. Tomov, M.B. Stuart, S.I. Nikolov, M.J. Pihl, Y. Du, J.H. Rasmussen, M. F. Rasmussen, J.A. Jensen, R.T. Nilsson, M. Hansen, U.D. Larsen, R.P. Domsten, B. G. Tomov, M.B. Stuart, S.I. Nikolov, M.J. Pihl, J.H. Rasmussen, M.F. Rasmussen, SARUS: a synthetic aperture real-time ultrasound system, Ieee Trans. Ultrason. Ferroelectr. Freq. Control. 60 (2013) 1838–1852, https://doi.org/10.1109/tuffc.2013.2770.

[27] G.-D. Kim, C. Yoon, S.-B. Kye, Y. Lee, J. Kang, Y. Yoo, T.-K. Song, A single FPGA-based portable ultrasound imaging system for point-of-care applications, Ieee Trans. Ultrason. Ferroelectr. Freq. Control. 59 (2012) 1386–1394, https://doi.org/10.1109/tuffc.2012.2339.

[28] J. Kang, C. Yoon, J. Lee, S.-B. Kye, Y. Lee, J.H. Chang, G.-D. Kim, Y. Yoo, T.-K. Song, A system-on-chip solution for point-of-care ultrasound imaging systems: architecture and ASIC implementation, Ieee T Biomed. Circ. S 10 (2016) 412–423, https://doi.org/10.1109/tbcas.2015.2431272.

[29] J. Kang, P. Kim, C. Yoon, Y. Yoo, T.-K. Song, Efficient parallel-beamforming based on shared FIFO for ultra-compact ultrasound imaging systems, Ieee Access 8 (2020) 80490–80501, https://doi.org/10.1109/access.2020.2990790.

[30] H. Kang, J. Kang, T. Song, Generalised dynamic decimation method using polyphase MACs for ultrasound imaging, Electron. Lett. 51 (2015) 451–452, https://doi.org/10.1049/el.2014.4133.

[31] P. Kim, J. Kang, T.-K. Song, A pseudo-dynamic delay calculation using optimal zone segmentation for ultra-compact ultrasound imaging systems, Electronics 8 (2019) 242, https://doi.org/10.3390/electronics8020242.

[32] P.J. Stolka, H.-J. Kang, M. Choti, E.M. Boctor, Multi-DoF Probe Trajectory Reconstruction with Local Sensors for 2D-to-3D Ultrasound, 2010 Ieee Int Symposium Biomed Imaging Nano Macro. (2010) 316–319. https://doi.org/10.1109/isbi.2010.5490347..

[33] J. Lee, J. Kang, T.-K. Song, 6-DOF Free-hand Navigation Interface for Volumetric 3-Dimensional Ultrasound Imaging: Preliminary Results, 2015 Ieee Int Ultrasonics Symposium Ius. (2015) 1–4. https://doi.org/10.1109/ultsym.2015.0297..

[34] L.V. Wang, Multiscale photoacoustic microscopy and computed tomography, Nat Photonics 3 (2009) 503–509, https://doi.org/10.1038/nphoton.2009.157.

[35] L.V. Wang, S. Hu, Photoacoustic tomography: in vivo imaging from organelles to organs, Science 335 (2012) 1458–1462, https://doi.org/10.1126/science.1216210.

[36] J. Kang, E. Kim, G.R. Kim, C. Yoon, T. Song, J.H. Chang, Photoacoustic imaging of breast microcalcifications: a validation study with 3-dimensional ex vivo data and

spectrophotometric measurement, J. Biophotonics 8 (2015) 71–80, https://doi.org/10.1002/jbio.201300100.

[37] J. Kang, J.H. Chang, S.M. Kim, H.J. Lee, H. Kim, B.C. Wilson, T.-K. Song, Real-time sentinel lymph node biopsy guidance using combined ultrasound, photoacoustic, fluorescence imaging: in vivo proof-of-principle and validation with nodal obstruction, Sci. Rep.-Uk 7 (2017) 45008, https://doi.org/10.1038/srep45008.

[38] H.-D. Chae, J.Y. Lee, J.-Y. Jang, J.H. Chang, J. Kang, M.J. Kang, J.K. Han, Photoacoustic imaging for differential diagnosis of benign polyps versus malignant polyps of the gallbladder: a preliminary study, Korean J. Radiol. 18 (2017) 821–827, https://doi.org/10.3348/kjr.2017.18.5.821.

[39] H.K. Zhang, Y. Chen, J. Kang, A. Lisok, I. Minn, M.G. Pomper, E.M. Boctor, Prostate-specific membrane antigen-targeted photoacoustic imaging of prostate cancer in vivo, J. Biophotonics 11 (2018) e201800021.

[40] J. Kang, E.M. Boctor, S. Adams, E. Kulikowicz, H.K. Zhang, R.C. Koehler, E. M. Graham, Validation of noninvasive photoacoustic measurements of sagittal sinus oxyhemoglobin saturation in hypoxic neonatal piglets, J. Appl. Physiol. 125 (2018) 983–989, https://doi.org/10.1152/japplphysiol.00184.2018.

[41] J. Kang, H.K. Zhang, S.D. Kadam, J. Fedorko, H. Valentine, A.P. Malla, P. Yan, M. M. Harraz, J.U. Kang, A. Rahmim, A. Gjedde, L.M. Loew, D.F. Wong, E.M. Boctor, Transcranial recording of electrophysiological neural activity in the rodent brain in vivo using functional photoacoustic imaging of near-infrared voltage-sensitive dye, Front. Neurosci.-Switz. 13 (2019) 579, https://doi.org/10.3389/fnins.2019.00579.

[42] J. Kang, S.D. Kadam, J.S. Elmore, B.J. Sullivan, H. Valentine, A.P. Malla, M. M. Harraz, A. Rahmim, J.U. Kang, L.M. Loew, M.H. Baumann, A.A. Grace, A. Gjedde, E.M. Boctor, D.F. Wong, Transcranial photoacoustic imaging of NMDA-evoked focal circuit dynamics in the rat hippocampus, J. Neural Eng. 17 (2020), 025001, https://doi.org/10.1088/1741-2552/ab78ca.

[43] J. Kang, X. Liu, S. Cao, S.R. Zeiler, E.M. Graham, E.M. Boctor, R.C. Koehler, Transcranial photoacoustic characterization of neurovascular physiology during early-stage photothrombotic stroke in neonatal piglets in vivo, J. Neural Eng. 18 (6) (2021) 065001, https://doi.org/10.1088/1741-2552/ac4596.

[44] W.G. Lesniak, Y. Wu, J. Kang, S. Boinapally, S.R. Banerjee, A. Lisok, A. Jablonska, E.M. Boctor, M.G. Pomper, Dual contrast agents for fluorescence and photoacoustic imaging: evaluation in a murine model of prostate cancer, Nanoscale 13 (2021) 9217–9228, https://doi.org/10.1039/d1nr00669j.

[45] Y. Wu, J. Kang, W.G. Lesniak, A. Lisok, H.K. Zhang, R.H. Taylor, M.G. Pomper, E. M. Boctor, System-level optimization in spectroscopic photoacoustic imaging of prostate cancer, Photoacoustics 27 (2022), 100378, https://doi.org/10.1016/j.pacs.2022.100378.